

Received January 17, 2021, accepted January 28, 2021, date of publication February 2, 2021, date of current version February 9, 2021.

Digital Object Identifier 10.1109/ACCESS.2021.3056561

Maritime Buoyage Inspection System Based on an Unmanned Aerial Vehicle and Active Disturbance Rejection Control

BAOYING LI¹, (Member, IEEE), SHENG GAO¹, CHEN LI^{1,2}, (Member, IEEE), AND HE WAN², (Student Member, IEEE)

¹School of Information Science and Engineering, Dalian Polytechnic University, Dalian 116034, China

²School of Electrical Engineering and Telecommunications, University of New South Wales, Sydney, NSW 2052, Australia

Corresponding author: Chen Li (chen.li1406@unsw.edu.au)


This work was supported in part by the Natural Science Foundation of Liaoning Province under Grant 2020-MS-274

ABSTRACT The unmanned aerial vehicle (UAV) is inexpensive and offers a fast response speed and robust flexibility; thus, it is a promising tool in the maritime buoyage inspection scenario, which involves monitoring and accessing a lateral mark system far away from the coast. However, two main problems can occur during inspection. The first is extreme weather conditions, resulting in a deviation between the inspection route and the design route. The second is that the buoyage beacons are visited only once. Therefore, this article proposes a buoyage inspection system consisting of a single UAV and random coastal buoys. The UAV automatically takes off from the depot, performs a self-check on the buoy beacons, and then returns to the depot. A cascade active disturbance rejection controller (ADRC) is designed to adjust the real-time trajectory of the UAV system. A feasible trajectory planning method is also designed based on the continuous Hopfield neural network (CHNN) and genetic algorithm (GA) to minimize the inspection distance. Extensive simulations are conducted to demonstrate the effectiveness of the proposed method.

INDEX TERMS Unmanned aerial vehicle, buoy inspection, active disturbance rejection control, continuous hopfield neural network, genetic algorithm.

I. INTRODUCTION

The coastal buoyage system provides accurate locations and safe navigation information for vessels [1], [2]. Due to the swaying of buoys and extreme weather conditions such as ocean breeze, strong waves, and thick mist, use of an autonomous underwater vehicle to inspect ocean buoys is impossible [3]. Buoyage inspection is one of the civil aviation scenarios [4]. With the maturing of UAVs, several advantages have been achieved, i.e., quick response [5], simple movement and operation [6], and high flexibility [7]; UAVs play a crucial role in monitoring buoys in the harbour and its adjoining water and coastal islands. As shown in Figure 1, a buoyage system consists on one UAV and several buoys. Supported by the advanced research in the control of autonomous UAVs, a UAV can inspect buoyage beacons by the following routine: launching from the depot, flying to buoys, inspecting beacons, and flying back to the depot. In addition, all buoys need to be visited only once, which can be regarded as a travelling salesman problem (TSP).

The associate editor coordinating the review of this manuscript and approving it for publication was Ailong Wu .

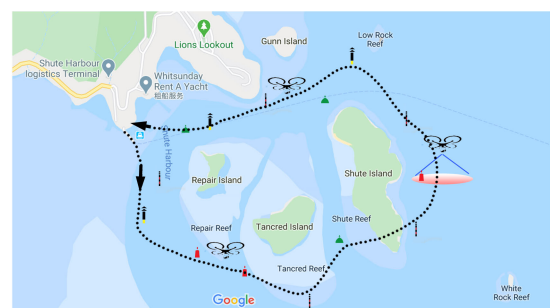


FIGURE 1. Buoy inspection system by using a UAV.

Compared to the traditional labour-intensive approach, UAVs require less time and cost and can enlarge the inspection area. The collision problem also exists in the inspection environment, especially the trajectory collision between a UAV and a buoyage target [8]. Moreover, there are two main problems in the UAV system: the trajectory tracking problem due to sudden wind in an uncertain environment and the problem of obtaining the shortest-distance trajectory.

The remainder of this article is organized as follows. Section II focuses on the analysis and a comparison with

different articles in trajectory tracking and path selection. The mathematical model of UAVs is established in Section III. The dual cascade ADRC used to track trajectories is designed in Section IV. A feasible trajectory planning strategy based on the continuous Hopfield neural network (CHNN) and genetic algorithm (GA) is designed in Section V. Section VI verifies the performances of the proposed method through MATLAB simulations. Finally, conclusions are given in Section VII.

A. CONTRIBUTION

This article's major contributions are twofold: (1) When a UAV meets an unknown disturbance in the ocean, the trajectory tracking performance is not accurate. Therefore, we propose the cascade dual ADRC closed-loop controller for monitoring and adjusting real-time flight routes. (2) A feasible path planning method based on the CHNN and genetic algorithm is designed to obtain the shortest-distance trajectory in which the buoy can be visited once.

II. RELATED WORK

Some effective control techniques have been reported for the trajectory tracking and path selection problems. However, some unknown influences can affect a UAV's stability, such as complex disturbances, model parameter perturbations, and unknown external disturbances (heavy wind gusts). Therefore, at least three methods have been proposed to tackle the above challenge. One method is robust PID control. For these circumstances, reference [9] developed the robust adaptive PID controller based on UAV fuzzy logic. In reference [10], the UAV's robust response in the presence of uncertainties and disturbances was guaranteed to satisfy the path tracking performance. Moreover, the UAV needed to carry a robust controller that could respond quickly to reduce the risk of terrific descent and drift from its original position [11]. In reference [12], the robust controller yielded an excellent dynamic response, a smaller tracking error, and an excellent robustness against unknown certainties, such as the actual ground effect and atmospheric disturbances. The second method, i.e., sliding mode control (SMC), has been employed in the UAV system. Compared with the robust PID control theory, SMC effectively eliminates the external disturbances and uncertainties, and it has strong robustness. However, it faces difficulty in reducing the effect of chattering, such as in reference [13], [14]. The current article corresponds to the third method, named the active disturbance rejection controller (ADRC). It estimates and compensates for the external disturbances and is independent of the model of the controlled object and insensitive to variations in the system parameters. As one of the robust control methods used to address uncertainty, the ADRC was first proposed by J.Q. Han in 1998 [15], [16]. The main idea of the ADRC theory is to treat the total disturbance as a new state variable and estimate it through an ESO [17]. As described in reference [18], the ADRC was used to adjust the angle and angular velocity in the UAV system automatically. Reference [19]

then applied the ADRC to reject perturbations generated by wind gusts, actuator faults, and measurement noises. The improved ESO in the ADRC can estimate these perturbations and compensate by the non-linear feedback control law. Additionally, reference [20] designed a feedback controller in the ADRC to eliminate the unmeasurable and external perturbations; this improved state feedback controller also ensures accurate trajectory tracking in the UAV system. Therefore, it is better to apply the ADRC to enhance the path tracking in buoy inspection.

Optimizing the flight trajectory via buoys is a traditional TSP in the UAV system, with variants such as the TSP with a UAV (TSP-D) [21], minimum cost TSP [22], TSP with a UAV station (TSP-DS) [23], and vehicle routing problem (VRP) [24]. J.J. Hopfield and Tank [25] first proposed solving the TSP by a feedback neural network in 1982, and they introduced the energy function to select the optimal path. However, the HNN easily converges to a valid solution or local minimum solution [26]. At least three methods were proposed to tackle this problem. One was the CHNN proposed in reference [27], but it could solve only part of the local minimum solution. An improved CHNN based on the dynamic step was proposed in reference [28] to calculate the feasible path. In addition, references [29] and [30] offered different optimization approaches. In reference [29], the authors considered a non-convex optimization problem with constraints on the joint UAV flight path planning and transmit power control, and they developed a successive-convex-approximation-based time minimization algorithm that simultaneously updates the UAV path and transmits power. In reference [30], the main problem is to carry out trajectory optimization by tailoring the successive convex approximation and alternating descent method to develop a joint trajectory and transmit power algorithm. Additionally, combining with path search algorithms such as the ant colony algorithm [31], genetic algorithm [32], Dijkstra [33], and A-star algorithm [34] was suggested to select the optimal trajectory without a local minimum solution. Thus, a novel method based on the CHNN can yield a better solution to the TSP.

III. UAV DYNAMIC MODEL ESTABLISHMENT

Normally, a UAV is actuated by quadrotors. There are two reference frames for analysing the UAV dynamic model: the earth-fixed frame $B = \{O_{xB}, O_{yB}, O_{zB}\}$ and the body-fixed frame $E = \{O_{xE}, O_{yE}, O_{zE}\}$. Moreover, the earth coordinate system is regarded as an inertial coordinate system. It assumes that the body-fixed frame and the centre of gravity of the UAV coincide and that its motion can be regarded as that of a rigid body with six degrees of freedom, including rotation around the yaw, pitch, and roll axes and three linear motions: forward and backward, left and right, and up and down. To describe the UAV performance, its absolute position vector is denoted as $[x, y, z]^T \in E$, and its attitudinal vector is denoted as the Euler angles $[\psi, \phi, \theta]^T \in E$. The Euler angles denote the yaw angle, the pitch angle and the roll angle, with

the assumption of $\psi \in [-\pi, \pi]$, $\phi, \theta \in [-\pi/2, \pi/2]$. Moreover, m denotes the mass of the UAV, g denotes the acceleration due to gravity, I_x, I_y, I_z denote the inertia moments in the body-fixed frame, and L denotes the distance from the rotor centre to the body centre of mass. U_1, U_2, U_3, U_4 are the speed inputs of the propellers, and $\Delta U_1, \Delta U_2, \Delta U_3, \Delta U_4$ are the changes in these inputs, respectively. The control forces and moments are generated by varying the speed of the rotors $\Omega_1, \Omega_2, \Omega_3, \Omega_4$. U_1 denotes the normalized total lift force along the z-axis, and U_2, U_3 , and U_4 correspond to the control inputs of the roll θ , the pitch ϕ and the yaw ψ moments, respectively. $U = [U_1, U_2, U_3, U_4]^T$ is the movement vector. $D_x, D_y, D_z, D_\phi, D_\theta, D_\psi$ are the disturbances outside the system. k_l denotes the lift coefficient of the UAV rotor, and k_f denotes the aerodynamic drag force coefficient in the UAV system. According to the Newton-Euler equation, the UAV mathematical model can be established, in which the angular motion is shown in (1), the transnational (vertical) motion is shown in (2), and the speed inputs (for the four propellers) are shown in (3). The overall structural model is shown in Figure 2.

$$\begin{cases} \ddot{\phi} = \dot{\theta}\dot{\psi} \left(\frac{I_y - I_z}{I_x} \right) + \frac{LU_2}{I_x} + D_\phi, \\ \ddot{\theta} = \dot{\psi}\dot{\phi} \left(\frac{I_z - I_x}{I_y} \right) + \frac{LU_3}{I_y} + D_\theta, \\ \ddot{\psi} = \dot{\phi}\dot{\theta} \left(\frac{I_x - I_y}{I_z} \right) + \frac{LU_4}{I_z} + D_\psi, \end{cases} \quad (1)$$

$$\begin{cases} \ddot{x} = (\sin \psi \sin \theta + \cos \psi \sin \phi \cos \theta) \frac{U_1}{m} + D_x, \\ \ddot{y} = (-\cos \psi \sin \theta + \sin \psi \sin \phi \cos \theta) \frac{U_1}{m} + D_y, \\ \ddot{z} = (\cos \theta \cos \phi) \frac{U_1}{m} - g + D_z, \end{cases} \quad (2)$$

$$\begin{cases} U_1 = k_l \left(\Omega_1^2 + \Omega_2^2 + \Omega_3^2 + \Omega_4^2 \right), \\ U_2 = k_l \left(\Omega_1^2 + \Omega_2^2 - \Omega_3^2 - \Omega_4^2 \right), \\ U_3 = k_l \left(\Omega_1^2 - \Omega_2^2 - \Omega_3^2 + \Omega_4^2 \right), \\ U_4 = k_f \left(\Omega_1^2 - \Omega_2^2 + \Omega_3^2 - \Omega_4^2 \right). \end{cases} \quad (3)$$

IV. TRAJECTORY TRACKING CONTROLLER DESIGN BASED ON ADRC SCHEME

This section mainly focuses on the trajectory tracking control subsystem based on the cascade active disturbance rejection controller (ADRC). Each ADRC is composed of three parts: an extended state observer (ESO), a tracking differentiator (TD) and a state error feedback control law (SEFCL). The structure of the overall control system is shown in Figure 3. The system inputs $U_i (i = 1, 2, 3, 4)$ ensure the trajectory tracking of $\{\phi, \theta, \psi, x, y, z\}$ along the desired trajectory $\{x_d, y_d, z_d\}$. There are four controlled channels: z vertical motion channel, ϕ channel, θ channel, and ψ channel. According to (1) and (2), the model of the transnational and vertical motions is determined by ϕ, θ, U_1 . \ddot{x} depends on ϕ and U_1 , \ddot{y} depends on θ and U_1 , and \ddot{z} depends on U_1 .

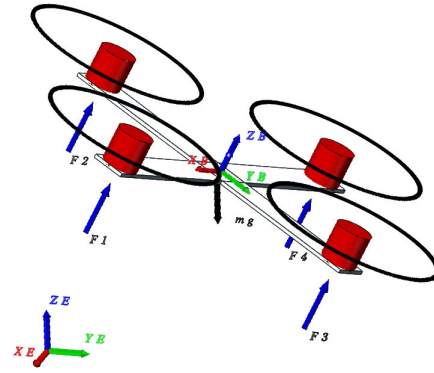


FIGURE 2. The overall structural model of a UAV: F_1 -the lift of the first motor, F_2 -the lift of the second motor, F_3 -the lift of the third motor, F_4 -the lift of the fourth motor, m -the mass of the UAV, g -the gravity of the UAV, O_{XYZb} -the body frame, and O_{XYZe} -the inertial frame.

Similarly, \ddot{x}, \ddot{y} are the input of the position loop in the angular motion model. ϕ, θ are controlled by U_2, U_3 . Moreover, the ADRC converts x_d, y_d, z_d into ϕ_d, θ_d, ψ_d , and it converts ϕ_d, θ_d, ψ_d into the current propeller speeds. The movement vector $U = [U_1, U_2, U_3, U_4]^T$ can act to change the UAV position. In addition, the yaw angle ψ control is considered as an example in this subsection. Recall that in (1), there is a coupling function $f(\dot{\phi}, \dot{\theta})$ between $\ddot{\psi}$ and $\dot{\phi}, \dot{\theta}$; thus, (1) needs to be simplified to (4). The function of the ESO is to track and estimate the yaw angle in real time. The disturbance $f(\dot{\phi}, \dot{\theta})$ is compensated for by the SEFCL.

$$\ddot{\psi} = f(\dot{\phi}, \dot{\theta}) + \frac{LU_4}{I_z} + D_\psi. \quad (4)$$

Take the ψ channel as an example. Let τ_D denote the filter time constant, and let k_D be a constant. G_e is the first-order transfer function of the UAV quadrotors in (5). We also need a decoupling transfer function G_m that represents the transfer function of the UAV dynamics (see (6)). Therefore, the transfer function of the ψ channel can be calculated as in (7), and the overall structure of the ADRC with the yaw angle is as shown in Figure 4.

$$G_e = \frac{k_D s}{\tau_D s + 1}, \quad (5)$$

$$G_m = \frac{LU_4}{I_z s^2}, \quad (6)$$

$$G_\psi = G_m \cdot G_e = \frac{LU_4}{I_z s^2} \cdot \frac{k_D s}{\tau_D s + 1}, \quad (7)$$

where $\tau_D = 0.0023$, $k_D = 0.09$, $I_z = 0.151$, and $L = 0.5$. We use the above parameters to obtain the transfer function of the ψ channel in (8).

$$G_\psi = \frac{0.5}{0.151 s^2} \cdot \frac{0.09 s}{0.0023 s + 1} = \frac{130}{s^2 + 435 s}. \quad (8)$$

Based on the above analysis, the ADRC can maintain trajectory tracking accuracy and compensate for the error of position shifting. The principle of the other channels is the same as for the ψ channel, and the transfer function of all channels is as shown in Table 1.

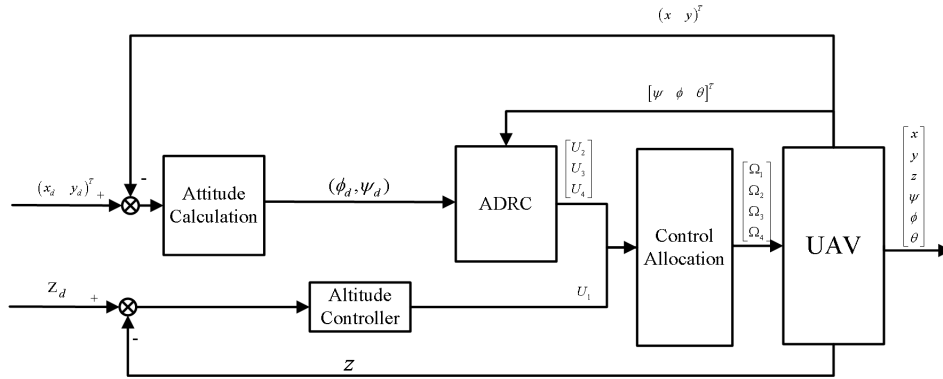


FIGURE 3. Block diagram of the overall control system. An altitude controller is used to convert the trajectory error into the desired roll, pitch and yaw angles.

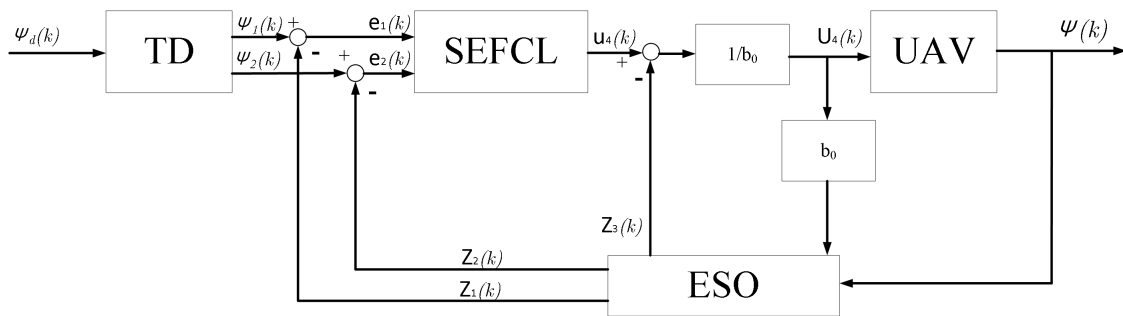


FIGURE 4. Block diagram of the ADRC in the yaw angle channel.

A. TRACKING DIFFERENTIATOR (TD)

A second-order TD is designed, as shown in (9). There are two transition signals $\psi_1(k)$ and $\psi_2(k)$. The tracking differentiator provides more stable and accurate results than numerical differentiation in the presence of noise [35].

$$\begin{cases} \psi_1(k+1) = \psi_1(k) + h\psi_2(k), \\ \psi_2(k+1) = \psi_2(k) + f \text{han}(\psi_1(k) - \psi_d(k), \psi_2(k), r_0, h_0), \end{cases} \quad (9)$$

where $\psi_d(k)$ is the input, $\psi_1(k)$ and $\psi_2(k)$ are the discrete outputs, k is the sampling step, and h_0 and r_0 are filter coefficients. The fhan function is defined in (10) [15], [16], [35].

$$\begin{cases} d = \gamma\eta^2, \\ a_0 = \eta x_2, \\ y = x_1 + a_0, \\ a_1 = \sqrt{d(d + 8|y|)}, \\ a_2 = a_0 + \frac{1}{2} \text{sign}(y)(a_1 - d), \\ a = (a_0 + y) \text{fsg}(y, d) + a_2(1 - \text{fsg}(y, d)), \\ \text{fsg}(a_3, a_4) = \frac{1}{2}(\text{sign}(a_3 + a_4) - \text{sign}(a_3 - a_4)), \\ \text{fhan}(x_1, x_2, \gamma, \eta) = -\gamma(a/d) \text{fsg}(a, d) - \gamma \text{sign}(a)(1 - \text{fsg}(a, d)). \end{cases} \quad (10)$$

Remark 1: The main purpose of the tracking differentiator (TD) is to address a discontinuous input signal or random

TABLE 1. The transfer function for each channel in the UAV system.

Channel	Transfer Function
θ	$G_\theta = \frac{301.4s + 768.5}{86s^2 + 4488s}$
ϕ	$G_\phi = \frac{215s + 593}{82.95s^2 + 4425s}$
z	$G_z = \frac{1.83}{s^2 + 4s}$
ψ	$G_\psi = \frac{130}{s^2 + 435s}$

disturbance in a measurement. Furthermore, the differential output of the TD and fhan function can generate the error signal and error differential signal of the transition process and realize fast position tracking without overshoot.

B. EXTENDED STATE OBSERVER (ESO) WITH THE fal FUNCTION

External disturbances and unknown noise comprise the total noise in the UAV system. An extended state observer (ESO) with the fal filter can be designed to suppress these noises, as in (11) [36], [37].

$$\begin{cases} \varepsilon_1(k) = z_1(k) - \psi(k), \\ z_1(k+1) = z_1(k) + h_1(z_2(k) - \beta_1\varepsilon_1(k)), \\ z_2(k+1) = z_2(k) + h_1(z_3(k) - \beta_2 \text{fal}(\varepsilon_1(k), \alpha_1, \delta)) + b_0u(k), \\ z_3(k+1) = z_3(k) - h_1\beta_3 \text{fal}(\varepsilon_1(k), \alpha_2, \delta), \end{cases} \quad (11)$$

where $z_1(k+1)$ and $z_2(k+1)$ are the estimated values, with $z_2(k+1)$ being the derivative of $z_1(k+1)$. Additionally, $z_3(k+1)$ denotes the overall estimated uncertainties in the UAV system and serves as a compensating term for ψ_d . Likewise in (11), $\varepsilon_1(k)$ is the control internal variable with the errors of estimation. We choose $\alpha_1 = 0.5$ and $\alpha_2 = 0.25$ for simulation, and $\beta_1, \beta_2, \beta_3$ are the positive observer gains. δ is the positive linear bandwidth of the non-linear function. b_0 denotes the controller gain. The non-linear *fal* function is given in (12).

The ESO does not depend on the disturbance model and does not require the disturbance to be measured. The ESO can compensate for the non-linear dynamics, model uncertainty and external disturbances. A non-linear uncertain object (new state variable) with a disturbance link is realized using non-linear state feedback.

Remark 2: The ESO can estimate and compensate for the error of the yaw angle ψ_d . Once the yaw angle is determined, x_d, y_d, z_d are also obtained, making it possible to realize real-time trajectory tracking. In addition, the controller gain b_{y0} can be decreased to accelerate the control response, which is proved in [38].

C. STATE ERROR FEEDBACK CONTROL LAW (SEFCL)

$$\begin{cases} e_1(k) = \psi_1(k) - z_1(k), \\ e_2(k) = \psi_2(k) - z_2(k), \\ u_4(k) = -f \text{han}(e_1(k), k_c e_2(k), r_1, h_1), \\ U_4(k) = (u_4(k) - z_3(k)) / b_0, \end{cases} \quad (12)$$

with

$$\begin{cases} s = \frac{1}{2} [\text{sign}(e + \delta) - \text{sign}(e - \delta)], \\ \text{fal}(e, \alpha, \delta) = \frac{e s}{\delta^{1-\alpha}} + |e|^\alpha \text{sign}(e) (1 - s), \end{cases} \quad (13)$$

where $e_1(k)$ and $e_2(k)$ are the estimation errors, $u_4(k)$ is the intermediate control input, and $U_4(k)$ is the final output of the system [15], [16], [35].

The system needs to adopt an appropriate compensation method to eliminate the error. In the state error feedback control law, the functions *fal* and *fan* are used to construct the non-linear controller, which is similar to the PID controller.

Remark 3: Note that decreasing b_0 accelerates the control response and that the system overshoot can be restrained by increasing the differential coefficient k_c , which is proved in [38].

Based on the analysis in Section III, it should be noted that the trajectory tracking ADRC can effectively compensate for the unknown model and external disturbance. The design of the trajectory tracking controller reduces the external destabilization and uncertainties in the UAV system. These disturbances, regarded as the total disturbance, are compensated for dynamically by the extended state observer (ESO). When the system encounters a large error, the small gain is used to reduce the overshoot; when there is a small error

in the system, a large gain is used to increase the rapidity. This adjustment is realized by the *fal* and *fan* functions. Therefore, the trajectory tracking ADRC has higher robustness and a stronger tracking ability, and its biggest advantage is that it can decouple and eliminate disturbances more effectively. The ADRC offers robustness to reduce all disturbances. Because of space limitations, the stability of the ADRC is proven in [39].

V. NAVIGATION ALGORITHM FOR SINGLE UAV BUOY INSPECTION

A. SHORTEST-DISTANCE TRAJECTORY PROBLEM

A buoyage inspection system is considered in Figure 1, consisting of a single UAV and some coastal buoyage beacons. Let $P(P \in N)$ denote the buoy position in the coastal area, and let $d_{xy}(t)$ denote the Euclidean distance between two buoys $(x, y \in P)$. The objective is to find a closed shortest path such that buoys can be visited one time to obtain the shortest trajectory in terms of time from the depot, inspect all buoys, and then return to the depot in the graph $\vartheta(P, \nu)$ such that the UAV does not violate the energy constraint. Therefore, the shortest distance trajectory (SDT) problem is proposed, which can also be formulated as a TSP.

B. CONTINUOUS HOPFIELD NEURAL NETWORK (CHNN) ALGORITHM

The continuous Hopfield neural network (CHNN) algorithm is an effective approach to solve the shortest trajectory distance problem, and its basic idea is to map the TSP to the CHNN and search for the optimal path solution automatically by dynamic evolution of the network state. A transposition matrix with $N \times N$ neurons is proposed, in which numerous neurons i or j ($i \neq j, i, j \in N$) exist. Each neuron can transmit its output to all other neurons and receive feedback from all other neurons at the same time [27]. Let $\omega_{xi,yj}$ denote the weight value from (x, i) to (y, j) , as shown in (14).

$$\omega_{xi,yj} = -A\delta_{x,y} (1 - \delta_{i,j}) - B\delta_{i,j} (1 - \delta_{x,y}) - C - Dd_{xy} (\delta_{j,i+1} + \delta_{j,i-1}), \quad (14)$$

where A, B, C and D represent the weighted values, which are all positive. $\delta_{i,j}$ and $\delta_{x,y}$ are both binary values, with $\delta_{i,j} = \begin{cases} 1 & (i = j) \\ 0 & (i \neq j) \end{cases}$ and $\delta_{x,y} = \begin{cases} 1 & (x = y) \\ 0 & (x \neq y) \end{cases}$. [40]

The energy function of the TSP needs to be considered. The key is to construct a suitable energy function E , as in (15). The energy function E can be composed of four parts. E_1 represents the first energy sub-function at the visiting order, E_2 is the second sub-function, E_3 is the global constraint function, and E_4 is the objective optimization target. The constraints E_1 and E_2 ensure that only one node can be visited at a time and that each node can be only accessed once. In addition, E_1 inhibits neurons after being visited many times, and E_2 inhibits neurons when accessing navigation marks simultaneously. E_4 is used to optimize the path length of the incentive network. Additionally, in the CHNN, the Sigmoid function is used as the activation function (16). Therefore, Algorithm 1 is

Algorithm 1 Constructing the Path via the CHNN

Require:

- The coordinates of the buoys;
- The distance $d_{xy}(t)$ between two buoys;

Ensure:

- One shortest path with minimum energy E ;
- 1: Initialize the weighted value A, B, C, D and u_0 ;
- 2: Calculate $d_{xy} (x \neq y, x, y \in N)$;
- 3: **for** CHNN **do**
- 4: Calculate $\frac{du_{x,i}}{dt}$ by Equation (9);
- 5: Calculate $u_{x,i} (t + 1)$ at time $t+1$;
- 6: Calculate $v_{x,i} (t)$;
- 7: Calculate the energy function E ;
- 8: **end for**

proposed to address the TSP with the CHNN.

$$\begin{cases} E = E_1 + E_2 + E_3 + E_4, \\ E_1 = \frac{A}{2} \sum_{x=1}^n \sum_{i=1}^n \sum_{j=1, j \neq i}^n v_{x,i} v_{x,j}, \\ E_2 = \frac{B}{2} \sum_{i=1}^n \sum_{x=1}^n \sum_{y=1, y \neq j}^n v_{x,i} v_{x,j}, \\ E_3 = \frac{C}{2} \left(\sum_{x=1}^n \sum_{i=1}^n v_{x,i} - n \right)^2, \\ E_4 = \frac{D}{2} \sum_{x=1}^n \sum_{y=1, y \neq x, i=1}^n d_{xy} v_{x,i} (v_{y,i+1} + v_{y,i-1}), \end{cases} \quad (15)$$

where $v_{x,i}$ indicates that buoy x is accessed in the i -th order. For example, if $v_{x,i} = 1$, buoy x will be visited in the i -th order; if $v_{x,i} = 0$, the opposite is true. Similarly, let $v_{x,j}$ indicate that buoy x is accessed in the j -th order, and let $v_{y,i+1}$ and $v_{y,i-1}$ indicate that buoy y is accessed in the $(i+1)$ -th and $(i-1)$ -th orders, respectively [41].

$$\begin{cases} v_{x,i} (t) = f(u_{x,i} (t)) = \frac{1}{2} \left(1 + \tanh \left(\frac{u_{x,i} (t)}{u_0} \right) \right), \\ u_{x,i} (t) = \frac{1}{2} u_0 \ln (n - 1) + \delta_{x,i} (x, i \in N), \\ u_{x,i} (t + 1) = u_{x,i} (t) + \frac{du_{x,i}}{dt} \Delta t, \end{cases} \quad (16)$$

where u_0 is the initial input, and $u_{x,i} (t)$ and $u_{x,i} (t + 1)$ indicate the inputs when the navigation mark x is visited in the i -th order at time t and $t+1$, respectively. $\delta_{x,i}$ has a random value within $(-1, 1)$ [42].

C. FEASIBLE ALGORITHM BASED ON THE CHNN AND GENETIC ALGORITHM

Although one feasible algorithm can be obtained through the CHNN, it is not reliable because the CHNN escapes from the local minimum solution with energy E to some extent. The general solution is to select a random order and adjust the weights of neurons $\omega_{xi,yj}$, but this can reduce the occurrence probability of the minimum value and cannot fundamentally

Algorithm 2 Constructing a Reliable and Feasible Path

Require:

- A random path transposition matrix;

Ensure:

- A feasible transposition matrix (feasible trajectory);

- 1: Initialize the weighted value A, B, C, D and u_0 ;
- 2: **while** $k_{ga} (k_{ga} \in N)$ **do**
- 3: Calculate $d_{xy} (x \neq y, x, y \in N)$;
- 4: **while** $k_{chnn} (k_{chnn} \in N)$ **do**
- 5: Calculate the energy function E by Algorithm 1;
- 6: **end while**
- 7: Calculate the current transposition matrix;
- 8: Calculate the fitness $\sum d_{xy}$ of the current path;
- 9: **if** The length of the current path is less than that of the parent path **and** the current path is an efficient solution **then**
- 10: Instead of the previous generation solution;
- 11: Calculate the input of the next CHNN;
- 12: **else**
- 13: Keep the previous generation solution;
- 14: The input of the CHNN remains unchanged;
- 15: **end if**
- 16: **end while**
- 17: Obtain the optimal generation;
- 18: Obtain the feasible and reliable inspection trajectory;

solve the global minimum problem. The relationship between the total UAV visiting sequence and the number of buoys can be restricted in the energy E , and it cannot restrict the situation where a UAV visits the same buoy many times or a UAV inspects multiple buoys at once, resulting in a minimum value in the sub-function E_3 . If the total visiting order is equal to the number of buoys, then $\sum_{x=1}^n \sum_{j=1}^n v_{xy} - n = 0$ in E_3 ;

if not, $\omega_{xi,yj}$ can be modified. Therefore, the feasible and reliable algorithm can be modified by the CHNN and genetic algorithm (GA) to solve the minimum value problem in E . Let $k_{ga} (k_{ga} \in N)$ and $k_{chnn} (k_{chnn} \in N)$ denote the iterations in the feasible and reliable algorithm. Algorithm 2 is presented to address the TSP, which is extended from Algorithm 1 by adding a genetic algorithm to the CHNN. This procedure ensures that the stored paths with minimum energy E are feasible and reduces the number of iterations needed to run the algorithm.

Algorithm 2 can be regarded as a feasible and reliable path planning algorithm, eliminating the local minimum solution in energy function E by an adaptive function and a selection function. It takes a random path transposition matrix and the random inspection trajectory as the CHNN input in Line 7. The individual adaptability function is formulated to judge the fitness of the current path matrix (or the current trajectory length), and this obtained path matrix can be taken as the parent sample. The new generation solution is generated at the same time in Line 8. In the genetic algorithm, from Line

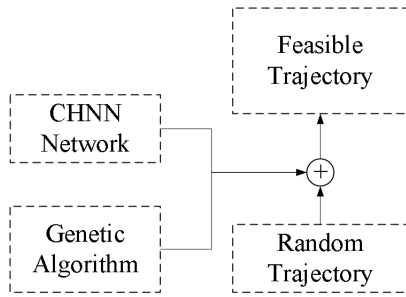


FIGURE 5. The overall structure of the feasible algorithm.

2 to 16, the current solution’s path length can be calculated by a selection function to obtain the sample with the highest fitness. For the variation factor, the CHNN randomly selects the weighted adjustment order. Even if the same input is used in the CHNN, some different training results are displayed. The variation factor is added to the generation solution. Finally, the feasible path can be counted, and the best one is selected as the final path matrix, that is, the optimal inspection trajectory for the UAV. The overall structure of the feasible algorithm for path planning is shown in Figure 5.

Now, the complexity of Algorithm 2 is analysed. It can be assumed that the maximum number of executions in the genetic algorithm is $|k_{ga}|$ (Line 2), and let $|k_{chmn}|$ denote the maximum number of executions in the CHNN (Line 4), where $k_{chmn} \neq k_{ga} \neq n$. Obviously, the most important time loss is caused by the CHNN. After calculating the energy function E (Line 5), it is necessary to judge whether the conditions meet the requirement. Therefore, the maximum execution time of the entire algorithm is $|k_{ga}| (|k_{chmn}| + 1)$. Overall, the total time complexity of Algorithm 2 is $O(|k_{ga}k_{chmn}| + |k_{chmn}|)$.

VI. NUMERICAL AND EXPERIMENTAL RESULTS

In this section, numerical and experimental results are given to verify the effectiveness of the proposed method under the superposition of external disturbances and model uncertainty, and a case study carried out in MATLAB is presented. The UAV used in the experiment is a laboratory product assembled by our group. Its parameters are shown in Table 2. All initial states of the considered UAV are set to zero, and the external disturbances and unknown certainties can be regarded as random white noise. A PC with an AMD Ryzen 7 3700x 8-Core Processor CPU @ 3.60 GHz and 32.00 GB of RAM is responsible for simulating the real-time angles and positions in the UAV system.

A. TRAJECTORY TRACKING CONTROL RESULTS

In this subsection, we mainly focus on the trajectory tracking control. The simulated parameters of the ADRC (ESO, TD, and SEFCL) and PID controller are given in Table 3. Additionally, in a UAV system, the total noise (i.e., the external disturbance and unknown model uncertainty) can be regarded as white Gaussian noise with zero mean, the sampling time is 0.5 s, and a variance of 15 is applied to describe the simulated noise. The UAV takes off and cruises during the process of

TABLE 2. Nominal parameters of the UAV.

Parameter	Value	Unit
g	9.81	m/s^2
I_x	0.085	kgm^2
I_y	0.083	kgm^2
I_z	0.151	kgm^2
L	0.5	m
m	1.3	kg
k_t	$2.85e^{-5}$	Ns^2
k_f	$7.47e^{-7}$	Ns^2
v	10	m/s

TABLE 3. Control parameters of the ADRC (TD, ESO, SEFCL) and PID controller.

ADRC-TD	r	h		
ψ	1000	0.002		
ϕ	1000	0.002		
θ	1000	0.002		
z	1000	0.002		
ADRC-ESO	h	b0	b1	
ψ	0.0514	3.4752	54.0801	
ϕ	0.0514	3.4752	54.0801	
z	1.83E-04	2.2715	18.7985	
ADRC-SFCL	r	h	kp	kd
ψ	944.6327	0.0289	100.023	0.0683
ϕ	944.6327	0.0289	0.0683	100.023
θ	944.6327	0.0289	0.0683	100.023
z	83.3269	0.0443	5.8124	2.2202
PID	P	I	D	Filter Coefficient (N)
ψ	254.4676	3740.486	-0.60223	422.5418
ϕ	60.15243	4947.394	0.080439	244.5837
θ	44.68166	3665.676	0.060518	246.2502
z	667.8137	2783.401	37.32134	388.5442

buoy inspection. A comparison between the ADRC and PID controller is performed in the same environment to verify the proposed controller’s superiority. Therefore, we analyse the signal tracking performance between the ADRC and PID controller, including the altitude, yaw angle, pitch angle, and roll angle; moreover, for the ADRC, the ESO output is analysed.

First, under the PID and ADRC control strategies, the tracking curves are plotted in Figure 6. We choose a random period for analysing the tracking performance, and the UAV meets a sudden change in wind force at $T = [0.5, 0.6]$. Regarding the rise time, the performance of the PID controller is worse than that of the ADRC in each channel, but the PID controller response is quicker than that of the ADRC. When the system meets an outside disturbance, the steady-state time of the PID controller is longer than that of the ADRC, and the overshoot of the PID controller is larger than that of the ADRC. For the pitch channel, the flight is smoother and more

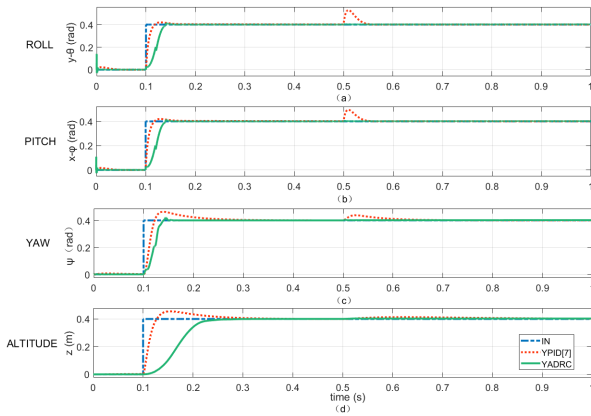


FIGURE 6. Outputs of the tracking signal for each channel: the input reference signal (blue dotted line), the tracking signal with the PID controller (red dotted line), and the tracking signal with the ADRC (green solid line).

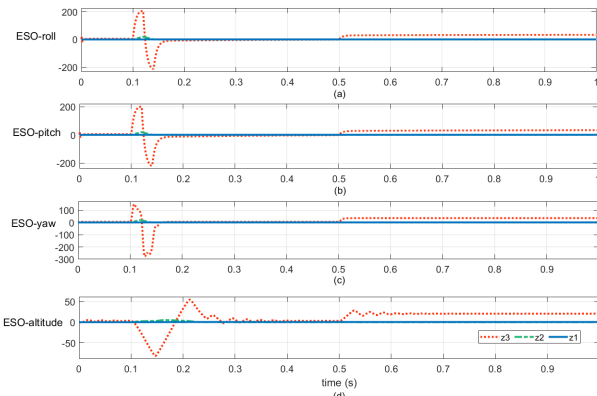


FIGURE 7. Outputs of the ESO for each channel: z_1 -the estimated disturbance of the input signal (blue solid line), z_2 -the estimated differential disturbance of the input signal (green dotted line), and z_3 -the estimated total disturbance (red dotted line).

steady with the ADRC than under PID control. Moreover, when there is an external disturbance, the ADRC can quickly adjust and track the UAV system’s real-time position. The case of the roll channel is similar to that of the pitch channel. For the yaw channel, the UAV maintains stable flight under the action of the ADRC. When the heading angle changes, the UAV can quickly and stably reach the specified yaw angle, while the PID controller results in overshoot. Therefore, under the influence of a gust disturbance, the ADRC has an outstanding tracking control ability compared with that of the PID controller.

We compare the output of the ESO in Figure 7. When an overshoot signal exists in the UAV system, the ESO estimates this as an error and compensates by using the ADRC to reduce it. Figure 7 shows that the ESO accurately estimates the disturbance value at $T = [0.5, 0.6]$ and utilizes the ADRC in time. We can observe that the UAV is under the control of complex disturbance factors when it performs the simulated inspection. The performance in terms of the attitude angles and altitude position fluctuates less under the ADRC, and the disturbance suppression ability is stronger than that of the

PID controller. Based on the analysis above, the ADRC is better than the PID controller in analysing the attitude angles and ESO performance.

B. NAVIGATION PATH SELECTION RESULTS

The effectiveness of the proposed algorithm and path tracking is verified in this subsection. Assume that the UAV can pass all buoys and ignore the influence of battery energy loss and that the UAV model parameters and the transfer functions of each channel remain unchanged. We choose a simulated coastal area with $12\text{ km} * 7\text{ km} * 0.005\text{ km}$ and randomly set 13 targets in this area. The depot is placed at (269, 293, 1). The flight trajectory needs to minimize the path of the UAV as it takes off from the depot, visits all buoys, and returns to the depot. The initial yaw angle ψ is set to 0 rad.

One path with the minimum solution as the reference is designed by Algorithm 2, and the ADRC tracks this trajectory. The simulation conditions of Algorithm 2 are set with k_{ga} and k_{chmn} . The fitness can be seen as the length of the trajectory. The UAV system sorts the different fitness values to select the highest fitness, i.e., the shortest path length.

In addition, Figure 8 shows the trajectory results simulated by using the CHNN-GA. An entirely random path is created initially, the length of which is 4171 m, as shown in Figure 8a. After 300 iterations in the CHNN, the path solution has the local minimum value, and the length of the current trajectory in the local minimum solution is 1915 m, as shown in Figure 8b. On this basis, the GA is combined with the CHNN to solve the local minimum solution in the CHNN. The path solution via the 3rd CHNN-GA can be observed in Figure 8c, with a length of 1944 m. Although the local minimum problem can be solved by selecting the stochastic direction of genetic variation, the minimum solution, not the local minimum solution, still exists, and the number of this kind of minimum solution can increase the number of nodes visited along the inspection trajectory. Repeating the CHNN and GA makes it possible to obtain the optimal path after the 9th CHNN-GA iteration, the length of which is 1825 m, as shown in Figure 8d. It can be seen that using only the CHNN to solve the TSP results in the local minimum solution; therefore, the CHNN is combined with the GA, with which the optimal path can be obtained. However, it is impossible to confirm whether the result obtained after the 9th genetic iteration is the optimal solution; it is necessary to look for the optimal path by using a genetic algorithm. The solution after the 13th GA iteration is shown in Figure 8e, and its length is 2088 m; the solution after the 67th GA iteration is also demonstrated in Figure 8f, the length of which is 1920 m. Because of the stochastic direction of genetic variation, the optimal solution can be selected by a sufficient number of mutation individuals, that is, the optimal solution is the shortest trajectory. Moreover, the energy corresponding to the optimal solution solved by the neural network is shown in Figure 8g, and the simulated trajectory’s path in each genetic iteration is shown in Figure 9b, in which the effective points are shown as stars (blue stars are the feasible solutions;

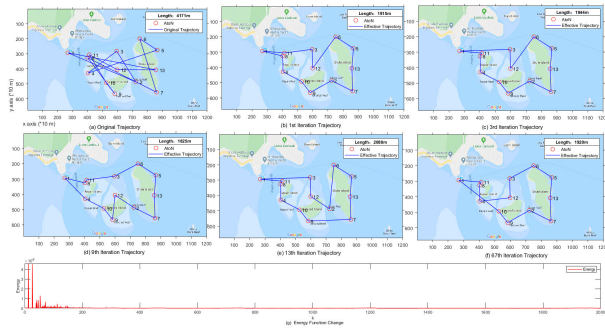


FIGURE 8. Experiment results for the CHNN: (a)-(c)+(f) the results obtained by using the CHNN, (d) the optimal solution, and (g) the energy output of the CHNN.

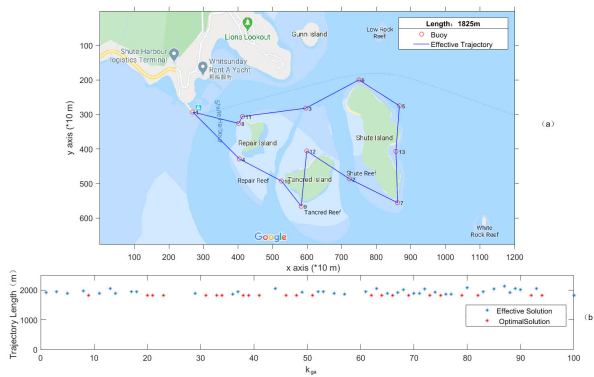


FIGURE 9. Experiment results for the feasible path planning algorithm: the buoy (the red circle), the desired and effective trajectory (the blue line), and the effective trajectory solution based on the genetic algorithm (the blue star).

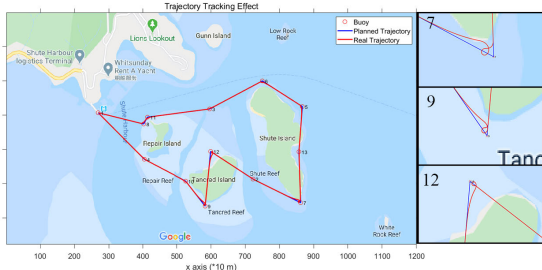


FIGURE 10. Experimental results for trajectory tracking: the actual tracking trajectory (the red line) and the actual flight trajectory for the 7,9,12-th buoyage target.

red stars are the optimal solutions). Therefore, it can be seen from Figure 9b that many optimal solutions can be obtained via the genetic iteration process.

Now, we analyse the ADRC performance, assuming that the UAV maintains a speed of 10 m/s. As shown in Figure 10, a comparison is made between the designed trajectory (solid blue line) and a real simulated trajectory; this solid blue line is the same as in Figure 10a. However, there are three specific buoys in the 7-th, 9-th and 12-th visiting sequences at which the UAV changes its yaw angle to adjust its attitude. Moreover, Figure 11 shows that the yaw angle changes in three time periods. The first one is between 92 s and 95 s (7-th); the second is between 125 s and 127 s (9-th), and the

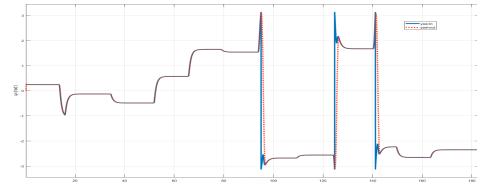


FIGURE 11. Experimental results for the yaw angle in the 7-th, 9-th, and 12-th visiting sequence: the desired yaw angle (the blue line) and the actual tracking yaw angle (the red dotted line).

last one is between 140 s and 142 s (12-th). Clearly, the ADRC can accurately track the x and y coordinates, and the tracking error is much smaller.

The buoyage inspection can be effectively implemented based on the proposed path planning algorithm and ADRC trajectory tracking performances.

VII. CONCLUSION

In this article, a coastal buoy inspection system is designed, including a UAV and several buoyage targets. The cascade ADRC controller realizes accurate trajectory tracking. Moreover, a feasible path planning algorithm based on the CHNN network and genetic algorithm is proposed. The ADRC controller has a strong anti-interference ability through MATLAB compared with the PID controller in the under strong disturbance and certain unknown environment. The proposed feasible path planning algorithm can effectively avoid the local minimum solution and obtain the shortest trajectory.

This article mainly proposes a method for improving the optimal path based on the CHNN and the UAV control by the cascade active disturbance rejection control algorithm. This method is mainly based on the actual engineering background of coastal navigation system inspection. Two real-world problems are solved: the need to overcome the complex disturbance environment along the coast and the need to find the optimal inspection route. In this article, through a MATLAB simulation, the robustness and control response of the improved cascade active disturbance rejection controller and the traditional PID controller are compared. From the experimental results, although the response of the active disturbance rejection controller is slower than that of the PID controller, its ability to compensate for disturbances is very prominent. On the other hand, due to the limitations of the CHNN-based method, the improved method solves the local minimum problem by integrating the GA method. The hybrid CHNN-GA can effectively avoid the minimum value problem and find the optimal inspection route from the experimental results.

REFERENCES

- [1] A. S. Lomax, W. Corso, and J. F. Etro, "Employing unmanned aerial vehicles (UAVs) as an element of the integrated ocean observing system," in *Proc. OCEANS MTS/IEEE*, Washington, DC, USA, Sep. 2005, pp. 184–190, doi: 10.1109/OCEANS.2005.1639759.
- [2] C. Trasviña-Moreno, R. Blasco, Á. Marco, R. Casas, and A. Trasviña-Castro, "Unmanned aerial vehicle based wireless sensor network for marine-coastal environment monitoring," *Sensors*, vol. 17, no. 3, p. 460, Feb. 2017, doi: 10.3390/s17030460.

- [3] H. Chen, F. Yin, W. Huang, M. Liu, and D. Li, "Ocean surface drifting buoy system based on UAV-enabled wireless powered relay network," *Sensors*, vol. 20, no. 9, p. 2598, May 2020, doi: [10.3390/s20092598](https://doi.org/10.3390/s20092598).
- [4] H. Huang and A. V. Savkin, "A method for optimized deployment of unmanned aerial vehicles for maximum coverage and minimum interference in cellular networks," *IEEE Trans. Ind. Informat.*, vol. 15, no. 5, pp. 2638–2647, May 2019, doi: [10.1109/TII.2018.2875041](https://doi.org/10.1109/TII.2018.2875041).
- [5] J. Tang, "Conflict detection and resolution for civil aviation: A literature survey," *IEEE Aerosp. Electron. Syst. Mag.*, vol. 34, no. 10, pp. 20–35, Oct. 2019, doi: [10.1109/MAES.2019.2914986](https://doi.org/10.1109/MAES.2019.2914986).
- [6] A. V. Savkin and H. Huang, "Range-based reactive deployment of autonomous drones for optimal coverage in disaster areas," *IEEE Trans. Syst., Man, Cybern. Syst.*, early access, Oct. 9, 2019, doi: [10.1109/TSMC.2019.2944010](https://doi.org/10.1109/TSMC.2019.2944010).
- [7] A. V. Savkin and H. Huang, "A method for optimized deployment of a network of surveillance aerial drones," *IEEE Syst. J.*, vol. 13, no. 4, pp. 4474–4477, Dec. 2019, doi: [10.1109/JSYST.2019.2910080](https://doi.org/10.1109/JSYST.2019.2910080).
- [8] J. Tang, M. A. Piera, and T. Guasch, "Coloured Petri net-based traffic collision avoidance system encounter model for the analysis of potential induced collisions," *Transp. Res. C, Emerg. Technol.*, vol. 67, pp. 357–377, Jun. 2016, doi: [10.1016/j.trc.2016.03.001](https://doi.org/10.1016/j.trc.2016.03.001).
- [9] A. Sarhan and S. Qin, "Robust adaptive flight controller for UAV systems," in *Proc. 4th Int. Conf. Inf. Sci. Control Eng. (ICISCE)*, Changsha, China, Jul. 2017, pp. 1214–1219, doi: [10.1109/ICISCE.2017.252](https://doi.org/10.1109/ICISCE.2017.252).
- [10] N. Katal, P. Kumar, and S. Narayan, "Design of $PI\Delta D\mu$ controller for robust flight control of a UAV using multi-objective bat algorithm," in *Proc. 2nd Int. Conf. Recent Adv. Eng. Comput. Sci. (RAECS)*, Chandigarh, India, Dec. 2015, pp. 1–5, doi: [10.1109/RAECS.2015.7453296](https://doi.org/10.1109/RAECS.2015.7453296).
- [11] M. K. Joyo, D. Hazry, S. F. Ahmed, M. H. Tanveer, F. A. Warsi, and A. T. Hussain, "Altitude and horizontal motion control of quadrotor UAV in the presence of air turbulence," in *Proc. IEEE Conf. Syst., Process Control (ICSPC)*, Kuala Lumpur, Malaysia, Dec. 2013, pp. 16–20, doi: [10.1109/SPC.2013.6735095](https://doi.org/10.1109/SPC.2013.6735095).
- [12] W. Rui, Z. Zhou, and S. Yanhang, "Robust landing control and simulation for flying wing UAV," in *Proc. Chin. Control Conf.*, Changsha, Hunan, Jul. 2006, pp. 600–604, doi: [10.1109/CHICC.2006.4346934](https://doi.org/10.1109/CHICC.2006.4346934).
- [13] H. Yin, Q. Wang, and C. Sun, "Position and attitude tracking control for a quadrotor UAV via double-loop controller," in *Proc. 29th Chin. Control Decis. Conf. (CCDC)*, Chongqing, China, May 2017, pp. 5358–5363, doi: [10.1109/CCDC.2017.7979449](https://doi.org/10.1109/CCDC.2017.7979449).
- [14] W. MacKunis, Z. D. Wilcox, M. K. Kaiser, and W. E. Dixon, "Global adaptive output feedback tracking control of an unmanned aerial vehicle," *IEEE Trans. Control Syst. Technol.*, vol. 18, no. 6, pp. 1390–1397, Nov. 2010, doi: [10.1109/TCST.2009.2036835](https://doi.org/10.1109/TCST.2009.2036835).
- [15] J. Han, "From PID to active disturbance rejection control," *IEEE Trans. Ind. Electron.*, vol. 56, no. 3, pp. 900–906, Mar. 2009, doi: [10.1109/TIE.2008.2011621](https://doi.org/10.1109/TIE.2008.2011621).
- [16] Z. Yin, C. Du, J. Liu, X. Sun, and Y. Zhong, "Research on autodisturbance-rejection control of induction motors based on an ant colony optimization algorithm," *IEEE Trans. Ind. Electron.*, vol. 65, no. 4, pp. 3077–3094, Apr. 2018, doi: [10.1109/TIE.2017.2751008](https://doi.org/10.1109/TIE.2017.2751008).
- [17] L.-X. Xu, H.-J. Ma, D. Guo, A.-H. Xie, and D.-L. Song, "Backstepping sliding-mode and cascade active disturbance rejection control for a quadrotor UAV," *IEEE/ASME Trans. Mechatronics*, vol. 25, no. 6, pp. 2743–2753, Dec. 2020, doi: [10.1109/TMECH.2020.2990582](https://doi.org/10.1109/TMECH.2020.2990582).
- [18] Y. Q. Shan, S. Wang, A. Konvisarova, and Y. J. Hu, "Attitude control of flying wing UAV based on advanced ADRC," in *Proc. IOP Conf., Mater. Sci. Eng.*, 2019, p. 677, doi: [10.1088/1757-899X/677/5/052075](https://doi.org/10.1088/1757-899X/677/5/052075).
- [19] Y. Guo, B. Jiang, and Y. Zhang, "A novel robust attitude control for quadrotor aircraft subject to actuator faults and wind gusts," *IEEE/CAA J. Automatica Sinica*, vol. 5, no. 1, pp. 292–300, Jan. 2018, doi: [10.1109/JAS.2017.7510679](https://doi.org/10.1109/JAS.2017.7510679).
- [20] A. Abadi, A. E. Amraoui, H. Mekki, and N. Ramdani, "Robust tracking control of quadrotor based on flatness and active disturbance rejection control," *IET Control Theory Appl.*, vol. 14, no. 8, pp. 1057–1068, May 2020, doi: [10.1049/iet-cta.2019.1363](https://doi.org/10.1049/iet-cta.2019.1363).
- [21] N. Agatz, P. Bouman, and M. Schmidt, "Optimization approaches for the traveling salesman problem with drone," *Transp. Sci.*, vol. 52, no. 4, pp. 965–981, Aug. 2018.
- [22] Q. M. Ha, Y. Deville, Q. D. Pham, and M. H. Hà, "On the min-cost traveling salesman problem with drone," *Transp. Res. C, Emerg. Technol.*, vol. 86, pp. 597–621, Jan. 2018.
- [23] S. Kim and I. Moon, "Traveling salesman problem with a drone station," *IEEE Trans. Syst., Man, Cybern. Syst.*, vol. 49, no. 1, pp. 42–52, Jan. 2019, doi: [10.1109/TSMC.2018.2867496](https://doi.org/10.1109/TSMC.2018.2867496).
- [24] K. Dorling, J. Heinrichs, G. G. Messier, and S. Magierowski, "Vehicle routing problems for drone delivery," *IEEE Trans. Syst., Man, Cybern. Syst.*, vol. 47, no. 1, pp. 70–85, Jan. 2017, doi: [10.1109/TSMC.2016.2582745](https://doi.org/10.1109/TSMC.2016.2582745).
- [25] W. Lin, J. G. Delgado-Frias, S. Vassiliadis, and G. G. Pechanek, "An investigation of the precision impact on the hopfield-tank neural network model for the TSP," in *Proc. IEEE Int. Conf. Neural Netw. (ICNN)*, Orlando, FL, USA, vol. 7, Jun. 1994, pp. 4523–4528, doi: [10.1109/ICNN.1994.375002](https://doi.org/10.1109/ICNN.1994.375002).
- [26] L. Tundong, Z. Huafei, and G. Yang, "Solving TSP via fuzzy dynamic PSO and HNN algorithm," in *Proc. 7th Int. Conf. Comput. Sci. Edu. (ICCSE)*, Melbourne, VIC, Australia, Jul. 2012, pp. 105–109, doi: [10.1109/ICCSE.2012.6295036](https://doi.org/10.1109/ICCSE.2012.6295036).
- [27] Z. Uykan, "On the working principle of the hopfield neural networks and its equivalence to the GADIA in optimization," *IEEE Trans. Neural Netw. Learn. Syst.*, vol. 31, no. 9, pp. 3294–3304, Sep. 2020, doi: [10.1109/TNNLS.2019.2940920](https://doi.org/10.1109/TNNLS.2019.2940920).
- [28] C. Zhong, C. Luo, Z. Chu, and W. Gan, "A continuous hopfield neural network based on dynamic step for the traveling salesman problem," in *Proc. Int. Joint Conf. Neural Netw. (IJCNN)*, Anchorage, AK, USA, May 2017, pp. 3318–3323, doi: [10.1109/IJCNN.2017.7966272](https://doi.org/10.1109/IJCNN.2017.7966272).
- [29] H. Wang, J. Wang, G. Ding, J. Chen, and J. Yang, "Completion time minimization for turning angle-constrained UAV-to-UAV communications," *IEEE Trans. Veh. Technol.*, vol. 69, no. 4, pp. 4569–4574, Apr. 2020, doi: [10.1109/TVT.2020.2976938](https://doi.org/10.1109/TVT.2020.2976938).
- [30] J. Gu, H. Wang, G. Ding, Y. Xu, Z. Xue, and H. Zhou, "Energy-constrained completion time minimization in UAV-enabled Internet of Things," *IEEE Internet Things J.*, vol. 7, no. 6, pp. 5491–5503, Jun. 2020, doi: [10.1109/JIOT.2020.2981092](https://doi.org/10.1109/JIOT.2020.2981092).
- [31] S. Konatowski and P. Pawlowski, "Ant colony optimization algorithm for UAV path planning," in *Proc. 14th Int. Conf. Adv. Trends Radioelectronics, Telecommun. Comput. Eng. (TCSET)*, Slavsk, Ukraine, Feb. 2018, pp. 177–182, doi: [10.1109/TCSET.2018.8336181](https://doi.org/10.1109/TCSET.2018.8336181).
- [32] Q. Yang and S.-J. Yoo, "Optimal UAV path planning: Sensing data acquisition over IoT sensor networks using multi-objective bio-inspired algorithms," *IEEE Access*, vol. 6, pp. 13671–13684, 2018, doi: [10.1109/ACCESS.2018.2812896](https://doi.org/10.1109/ACCESS.2018.2812896).
- [33] L. Deng, H. Yuan, L. Huang, S. Yan, and Y. Lai, "Post-earthquake search via an autonomous UAV: Hybrid algorithm and 3D path planning," in *Proc. 14th Int. Conf. Natural Comput., Fuzzy Syst. Knowl. Discovery (ICNCFSKD)*, Huangshan, China, Jul. 2018, pp. 1329–1334, doi: [10.1109/FSKD.2018.8687272](https://doi.org/10.1109/FSKD.2018.8687272).
- [34] M. H. Erol and F. Bulut, "Real-time application of travelling salesman problem using Google maps API," in *Proc. Electr. Electron., Comput. Sci., Biomed. Eng. Meeting (EBBT)*, Istanbul, Turkey, Apr. 2017, pp. 1–5, doi: [10.1109/EBBT.2017.7956764](https://doi.org/10.1109/EBBT.2017.7956764).
- [35] J. Q. Han and W. Wang, "Nonlinear tracking differentiator," (in Chinese), *J. Syst. Sci. Math. Sci.*, vol. 14, no. 2, 1994, pp. 177–183.
- [36] A. Jaballaafou, A. A. Madi, A. Addaim, and A. Intidam, "Wind power production based on DFIG: Modeling and control by ADRC," in *Proc. IEEE 20th Medit. Electrotech. Conf. (MELECON)*, Palermo, Italy, Jun. 2020, pp. 517–522, doi: [10.1109/MELECON48756.2020.9140611](https://doi.org/10.1109/MELECON48756.2020.9140611).
- [37] Z.-P. Gao, X.-R. Song, C.-B. Chen, S. Gao, F. Qian, and P.-F. Ren, "The study for path following of robot fish based on ADRC," in *Proc. IEEE Int. Conf. Unmanned Syst. Artif. Intell. (ICUSAI)*, Xi'an, China, Nov. 2019, pp. 194–199, doi: [10.1109/ICUSAI47366.2019.9124758](https://doi.org/10.1109/ICUSAI47366.2019.9124758).
- [38] X. H. Wang, Z. Q. Chen, and Z. Z. Yuan, "Output tracking based on extended observer for nonlinear uncertain systems," (in Chinese), *J. Control Decis.*, vol. 19, no. 10, pp. 1113–1116, 2004, doi: [10.13195/j.cd.2004.10.34.wangxh.008](https://doi.org/10.13195/j.cd.2004.10.34.wangxh.008).
- [39] J. Zhang, X. Yang, Y. X. Liu, and X. X. Yao, "Performance evaluation for active disturbance rejection with high-order line extended state observer," (in Chinese), *J. Control Decis.*, vol. 30, no. 7, 2015, pp. 1162–1170, doi: [10.13195/j.kzyjc.2014.0563](https://doi.org/10.13195/j.kzyjc.2014.0563).
- [40] Y. He and L. Wang, "Chaotic neural networks and their applications," in *Proc. 3rd World Congr. Intell. Control Autom.*, Hefei, China, vol. 2, 2000, pp. 826–830, doi: [10.1109/WCICA.2000.863345](https://doi.org/10.1109/WCICA.2000.863345).
- [41] P. Wang, L. Wang, H. Leung, and G. Zhang, "Subpixel mapping based on hopfield neural network with more prior information," *IEEE Geosci. Remote Sens. Lett.*, vol. 16, no. 8, pp. 1284–1288, Aug. 2019, doi: [10.1109/LGRS.2019.2895629](https://doi.org/10.1109/LGRS.2019.2895629).

[42] A. D. Vita, D. Pau, C. Parrella, L. D. Benedetto, A. Rubino, and G. D. Licciardo, "Low-power HWAccelerator for AI edge-computing in human activity recognition systems," in *Proc. 2nd IEEE Int. Conf. Artif. Intell. Circuits Syst. (AICAS)*, Genova, Italy, Aug. 2020, pp. 291–295, doi: 10.1109/AICAS48895.2020.9073913.



BAOYING LI (Member, IEEE) was born in 1965. He received the B.E. and M.E. degrees with the Dalian Institute of Light Industry (now Dalian Polytechnic University), in 1988 and 1994, respectively. He is currently an Associate Professor with Dalian Polytechnic University. His research interests include intelligent control and its application in unmanned systems.



SHENG GAO received the B.E. degree in automation from Dalian Polytechnic University, in 2019, where he is currently pursuing the M.E. degree. He works with control theory. His research interests include machine learning and control theory.



CHEN LI (Member, IEEE) was born in Dalian, China, in 1994. He received the M.Eng.Sc. degree from the School of Electrical Engineering and Telecommunications, University of New South Wales (UNSW), Australia, in 2019. He is currently a Research Assistant with the Research Centre for Integrated Transport Innovation, UNSW, Sydney. His current research interest includes the theory and application of guidance, navigation, and control. He has served as an Invite Reviewer for several top journals, such as *IET Signal Processing*, the *IEEE ASIAN JOURNAL OF CONTROL*, and the *International Journal of Advanced Robotic Systems*.



HE WAN (Student Member, IEEE) received the B.S. degree in automation from Beihang University, Beijing, China, in June 2017. He is currently pursuing the M.S. degree with the School of Electrical Engineering and Telecommunications, University of New South Wales, Sydney, Australia. His research interests include mobile robot control and machine learning.

...